Nonunique fraction of Fock exchange for defects in two-dimensional materials

Wei Chen,[1] Sinéad M. Griffin,[2,3] Gian-Marco Rignanese,[1] and Geoffroy Hautier[1,4]

[1] *Institute of Condensed Matter and Nanoscicence (IMCN), Université catholique de Louvain, Louvain-la-Neuve 1348, Belgium*
[2] *Molecular Foundry Division, Lawrence Berkeley National Laboratory, Berkeley, California 94720, USA*
[3] *Materials Sciences Division, Lawrence Berkeley National Laboratory, Berkeley, California 94720, USA*
[4] *Thayer School of Engineering, Dartmouth College, Hanover, New Hampshire 03755, USA*

(Dated: October 11, 2022)

By investigating the vacancy and substitutional defects in monolayer WS_2 with hybrid functionals, we find that there is no unique amount of Fock exchange that concurrently satisfies the generalized Koopmans' condition and reproduces the band gap and band-edge positions. Fixing the mixing parameter of Fock exchange based on the band gap can lead to qualitatively incorrect defect physics in two-dimensional materials. Instead, excellent agreement is achieved with both experiment and many-body perturbation theory within the *GW* approximation once the mixing parameters are tuned individually for the defect species and the band edges. We show the departure from a unique optimized mixing parameter is inherent to two-dimensional systems as the band edges experience a reduced screening whilst the localized defects are subject to bulklike screening.

Two-dimensional (2D) materials are rapidly gaining ground in a range of technologies owing to both their exotic electronic and optical properties due to quantum confinement [1] and the increasing ease of manipulation of their properties on a layer-by-layer basis. Defects have been shown to be viable active sites for enabling electrocatalysis (e.g., hydrogen evolution [2–4]) on otherwise inert basal planes of 2D materials. In quantum information science, 2D materials hold exceptional promise as defect hosts because their associated point defects typically present high spin states and deep defect levels [5–7], and any near-surface defects are easier to manipulate and characterize. The nature of such quantum defects is often elusive from experiment, and reliable theoretical modeling is required to understand their atomistic origins [8, 9]. First-principles defect calculations are now typically carried out with hybrid density functionals, the accuracy of which is closely related to the amount of Fock exchange admixed with semilocal exchange in the framework of generalized Kohn-Sham density-functional theory (DFT) [10]. The mixing parameter of hybrid functionals is commonly determined on the basis of the band gap of host systems from experiment or higher levels of theory. It has been well validated that such band-gap optimized mixing parameters lead to accurate defect levels for localized point defects in bulk materials [11].

The success of hybrid functionals can be attributed to the fulfillment of generalized Koopmans' condition, which for a localized defect, requires that the ionization energy and electron affinity to be equal, hence recovering the exact piecewise linearity of the total energy upon electron occupation [12–15]. Indeed, one can often find a single mixing parameter that describes the host band gap and the defect localization equally well in bulk materials [16]. The uniqueness of optimal mixing parameter promotes the use of a fixed, band-gap targeted mixing parameter in state-of-the-art defect calculations [10]. The same approach has been routinely applied to understand the defect properties in 2D materials [17–20]. In this Letter, we show that, in contrast to bulk 3D materials, there exists no unique amount of Fock exchange that can reproduce the experimental band gap and satisfying Koopmans' conditions for the defect level concurrently. Admixing a single fraction of Fock exchange thus could entail large errors in defect energy levels for 2D materials. We show that imposing appropriate mixing parameters individually for defects and host band edges is needed for an accurate description of defect energy levels, and discuss the failure of the typical hybrid-functional defect computation scheme.

To illustrate this issue, we investigate various point defects in monolayer (ML) WS_2, including the sulfur monovacancy (V_S), the single cobalt atom substituting sulfur (Co_S) or tungsten (Co_W), and the single carbon atom substituting sulfur (C_S). Several of these defects have recently become the subject of increasing theoretical and experimental efforts following the demonstrated quantum light emitters in 2D transition-metal dichalcogenides (TMDs) [21–26], and so are well-motivated for further consideration here [19, 27–29].

Our analysis of Koopmans' condition is primarily carried out using a global hybrid functional in which a single mixing parameter (α) controls the amount of Fock exchange admixed with the semilocal Perdew-Burke-Ernzerhof (PBE) exchange [30]. At $\alpha = 0.25$ this global hybrid functional is essentially the PBE0 functional [31, 32]. Conventionally we refer to this family of one-parameter hybrid functionals as PBE0(α). All hybrid-functional calculations are performed with the projector-augmented-wave method [33] as implemented in VASP [34, 35]. As a higher level of theory, many-body perturbation theory within the *GW* approximation [36, 37] is used to establish an accurate reference for the hybrid functional. Specifically, on top of

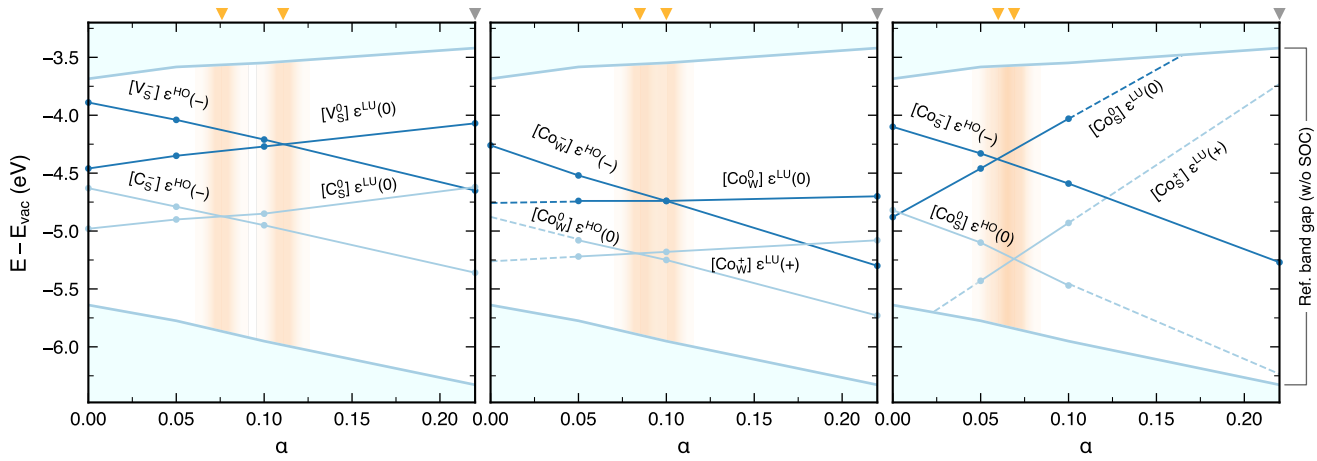

FIG. 1. Single-particle defect levels as a function of mixing parameter α for various defects in the ML WS_2. The eigenvalues are evaluated at the four representative α values shown by the solid dots and interpolated in between (solid lines). Linear extrapolations (indicated by dashed lines) are used when the localized defect state cannot be stabilized within the band gap. The band edges of ML WS_2 are indicated by the blue shades. All energies are referred to the vacuum level. The orange marker indicates the mixing parameter α_K at which the generalized Koopmans' condition $\varepsilon^{HO}(q) = \varepsilon^{LU}(q+1)$ is fulfilled, whereas the grey marker indicates the optimal mixing parameter ($\alpha_G = 0.22$) for reproducing the band gap of ML WS_2. Spin-orbit coupling (SOC) is not taken into account.

a PBE starting point, one-shot G_0W_0 calculations are performed for the ML WS_2 and some selected defects. The truncated Coulomb interaction [38] and the subsampling technique [39] are used to address the slow convergence of quasiparticle (QP) energies specific to 2D systems [40]. The G_0W_0 calculations are performed with BERKELEYGW [41] interfaced to the DFT code from Quantum-ESPRESSO [42]. The details of computational parameters for the hybrid-functional and G_0W_0 calculations are provided in the Supplemental Material (SM) [43].

We first survey the electronic structure of the pristine ML WS_2. Obtained from exfoliating 2H-WS_2, the ML WS_2 is a direct-gap semiconductor with a K–K transition. As a result of the trigonal prismatic crystal field splitting, the valence band maximum (VBM) is of $d_{x^2-y^2}$ and d_{xy} character whereas the conduction band minimum (CBM) is of d_{z^2} character. The G_0W_0 band gap of the ML WS_2 is 2.9 eV without SOC. To reproduce this reference G_0W_0 band gap, we find that the mixing parameter (dubbed as α_G) needs to be adjusted to 0.22 for the hybrid functional. Once the SOC is included, this PBE0(α_G) functional leads to a band gap of 2.58 eV, in good agreement with the experimentally reported values ranging from 2.4 to 2.7 eV [27, 44, 45]. We note that the experimental determination of the band gap is subject to the dielectric screening effect arising from the substrate [46, 47].

To identify the mixing parameter fulfilling the generalized Koopmans' condition for a given localized defect D, we calculate the single-particle eigenvalue $\varepsilon^{HO}(q)$ associated with the highest occupied (HO) state at charge state q as well as the eigenvalue $\varepsilon^{LU}(q+1)$ of the lowest unoccupied (LU) state at charge state $q+1$. The optimal mixing parameter α_K is determined when the equality $\varepsilon^{HO}(q) = \varepsilon^{LU}(q+1)$ holds. To calculate this we consider candidate defects embedded in an orthorhombic supercell of 90 atoms representing the ML WS_2. In particular, we refer the band edges and single-particle defect eigenvalues to the vacuum level, which is a natural and physical choice for 2D systems [18]. While the alignment is straightforward for neutral defects, the single-particle levels of charged defects are subject to finite-size effect arising from the spurious electrostatic interactions [11, 48–50]. The alignment is further complicated by the fact that the electrostatic potential in the vacuum region experiences an artificial bending due to the dipole moment introduced by the neutralizing charge background. Here we apply the potential correction scheme of Chagas da Silva *et al.* [51], thereby achieving well-defined single-particle eigenvalues with respect to vacuum for charged defects.

Figure 1 depicts the evolution of band edges and single-particle defect eigenvalues with respect to the mixing parameter α. The defect eigenvalues are obtained by linear interpolations or extrapolations based on the eigenvalues calculated at four α values (0, 0.05, 0.10, and 0.22). At a given α, the defect structure upon which the Koopmans' condition is assessed corresponds to the equilibrium structure of the charged state. At this stage, we do not take into account SOC for geometric relaxations and hence the determination of α_K due to its computational complexity. For all defects considered, the values of α_K fulfilling the Koopmans' condition are found in a narrow

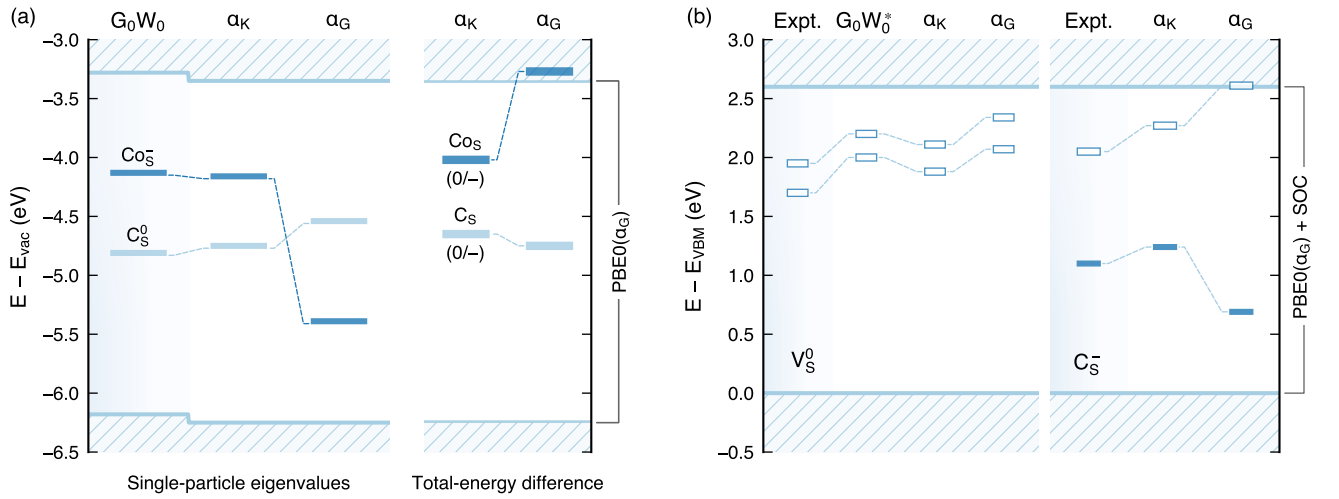

FIG. 2. (a) Defect levels of Co_S^{-1} and C_S^0 obtained with single-particle eigenvalues and total-energy difference with respect to the vacuum level. For each computational scheme, the PBE0(α) defect levels are calculated with α_K and α_G and are benchmarked against the G_0W_0 reference. To exclude the effect of structural relaxation, we use the PBE equilibrium structures throughout. The PBE0 band-edge positions are determined by PBE0(α_G). (b) Calculated single-particle defect levels with PBE0(α_K) and PBE0(α_G) compared to STS measurements for V_S^0 and C_S^-. The structures are relaxed with the corresponding α values for the PBE0 calculations. The defect levels are referred to the VBM and take into account the SOC. The band gap takes the value as obtained with PBE0(α_G)+SOC throughout. The G_0W_0 results (denoted by $G_0W_0^*$) are taken from Ref. 27.

range between 0.06 and 0.11, significantly lower than the band-gap enforced mixing parameter α_G of 0.22. We note that α_K values are largely unaffected by SOC as the Koopmans' condition is still fulfilled within 0.1 eV when SOC is included (see Table S1 of the SM). This is our first key result. Indeed, PBE(α_G) exhibits strong concavity as the ionization energy $-\varepsilon^{HO}(q)$ is consistently larger than the electron affinity $-\varepsilon^{LU}(q+1)$ for any given defect [52]. This is clearly at odds with the existence of a unique mixing parameter for bulk materials which is able to describe the band gap reasonably well without compromising the Koopmans' condition for localized defects [16, 53–55].

Among all defects considered, the effect of mixing parameter is particularly notable for Co_S. The defect levels associated with Co_S are predominately characterized by the strongly localized Co-3d states. Specifically, the (0/−) and (+/0) transitions involve the $d_{x^2-y^2}$ and the d_{z^2} orbitals of the Co atom, respectively. Taking the neutral Co_S^0 for example, we notice that the occupied d_{z^2} and unoccupied $d_{x^2-y^2}$ defect levels move sharply towards the host band edges as α increases and eventually merge into the valence and conduction band when $\alpha = \alpha_G$ (cf. Fig. 1). Consequently, PBE0(α_G) would predict that no localized defect levels exist within the band gap for Co_S, qualitatively at variance with the deep levels obtained with PBE0(α_K).

To settle the conflicting results of Co_S due to the choice of α, we carry out one-shot G_0W_0 calculations for the spin-unpolarized Co_S^- defect (see the SM for computational details). We find excellent agreement between the PBE0(α_K) and G_0W_0 defect levels (mainly of $d_{x^2-y^2}$ and d_{xy} characters of Co) [cf. Fig. 2(a)]. Both methods place the single-particle defect level −4.1 eV below the vacuum level, or equivalently about 2.1 eV above the VBM. By contrast, PBE0(α_G) overestimates the defect ionization energy by nearly 1.3 eV, consistent with the strong concavity noted previously in Fig. 1. The high accuracy of PBE0(α_K) is further demonstrated for C_S^0 [cf. Fig. 2(a)], while PBE0(α_G) still underperforms, albeit to a lesser extent than for Co_S^-.

An arguably more common approach to the determination of defect levels is through the total-energy difference between different defect charge states [10]. When referred to the VBM of the pristine host, the (0/−) charge transition level of defect D can be obtained as $E_{tot}(D^-) - E_{tot}(D^0) - E_{VBM}$. Analogous to the single-particle level, the total energy of charged defects are ill-defined for periodic systems. Here we apply the finite-size correction scheme of Komsa *et al.* [50, 56] as implemented in SLABCC [57] to the total energy of charged defect. The computed (vertical) (0/−) charge transition levels are shown in Fig. 2(a) for Co_S and C_S. In general, defect levels obtained with the total-energy difference scheme are less sensitive to the amount of Fock exchange when aligned to a common reference (e.g., average electrostatic potential or vacuum) [58–61]. While this is the case for the (0/−) level of C_S, for Co_S the agreement with the G_0W_0 QP energy found with PBE0(α_K) is substantially worse if α_G is used instead.

Our results so far suggest that fixing the α value, which is typically chosen based on the host band gap for studying defects in bulk materials, can be problematic and

even qualitatively change the defect physics in 2D materials. The discernible discrepancy between α_G and α_K suggests that defect levels need to be treated individually from band edges, the alignment of which can be easily achieved through the common vacuum level. To illustrate the validity the proposed scheme, we refer to to the scanning tunneling spectroscopy (STS) measurements of the neutral V_S^0 [27] and the negatively charged C_S^- [29] in Fig. 2(b). To facilitate the comparison, we include SOC in the hybrid-functional calculations and focus on the single-particle eigenvalues with the equilibrium defect structure at the charge state pertinent to experiment. The STS spectra revealed two prominent peaks at 1.8 eV and 2.0 eV above the VBM for V_S^0 [27]. The peaks correspond to the unoccupied d_{xy} and $d_{x^2-y^2}$ orbitals of the W atoms near the vacancy, whose degeneracy is lifted by spin-orbit splitting [17]. The positions of the two defect levels are well reproduced by the single-particle defect energies of our PBE0(α_K) calculations in reference to the band edges obtained with PBE0(α_G), and the accuracy is comparable to that of the G_0W_0 calculation of Ref. [27]. The C_S^- is also characterized by two defect levels deep within the band gap [29]. The two levels are mainly of the C-p_z character, with one occupied at 1.1 eV and the other unoccupied at 2.0 eV above the VBM. The importance of enforcing the Koopmans' condition is again evidenced for C_S^- as the splitting of the two defect levels would be too large if the mixing parameter is fixed at α_G.

To rationalize the departure from the existence of a unique α value as for bulk materials, we turn to the bulk WS_2 and examine the defect levels therein. The bulk 2H-WS_2 comprises repeated layers of ML WS_2, and has an indirect (Γ–K) band gap of 1.3 eV [62, 63]. The markedly smaller band gap leads to a strongly reduced mixing parameter α_G^{bulk} of 0.07. Defects are introduced to an orthorhombic supercell containing 72 atoms, which is based on the 36-atom supercell of the ML WS_2 comprising two alternating MLs stacked along the out-of-plane direction. Figure 3(a) shows the single-particle defect levels at the respective values of α_K for defects in both bulk and ML WS_2. Some defects such as Co_W no longer exhibit deep levels in the bulk WS_2. Interestingly, irrespective of the dimensionality of the host material, the various α_K values fall closely in the vicinity of α_G^{bulk}. The consistency in the α_K values implies that the localization of defect in the ML WS_2 is comparable to that of the bulk. This is clearly demonstrated in Fig. 3(b) where the defect charge density $\rho(D^q)-\rho(D^0)$ is plotted for the ML and the bulk host. Particularly for Co_S^- and C_S^-, the charge density along the in-plane direction is nearly intact when going from the bulk to the ML WS_2. The charge density analysis additionally provides an avenue to understand the screening effect. In the presence of a strictly localized defect, the average charge density approaches the delocalized screening charge density $(1-1/\epsilon)q/\Omega$ far away

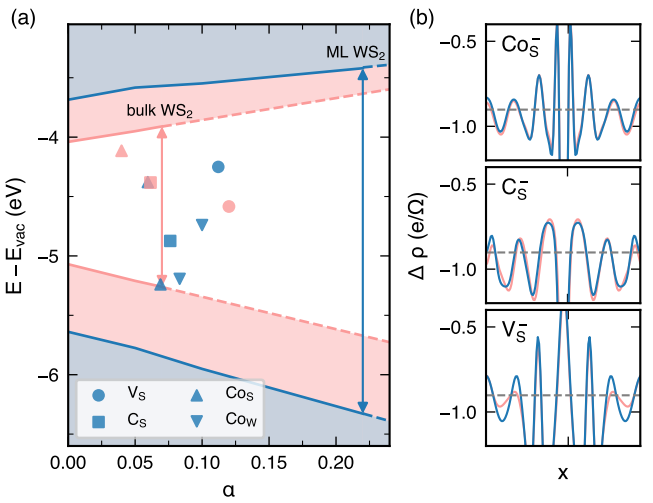

FIG. 3. (a) Single-particle defect levels at the Koopmans-fulfilled α_K in the monolayer (blue) and the bulk (red) WS_2. The band-edge positions of the monolayer and the bulk WS_2 are shown accordingly by the same color scheme. (b) Defect charge density $\rho(D^q)-\rho(D^0)$ of Co_S^-, C_S^-, and V_S^- as obtained with PBE along the in-plane direction in the monolayer (blue) and the bulk (red) WS_2. The horizontal line refers to the delocalized screening charge density $(1-1/\bar{\epsilon})q/\Omega$ given a localized defect at charge state q where $\bar{\epsilon}$ stands for the averaged dielectric constant of the bulk WS_2. The defects are situated near the center.

from the defect [49], where ϵ is the dielectric constant and Ω the volume of the supercell. Using the (geometrically) averaged dielectric constant ($\bar{\epsilon}=10.2$) of the bulk WS_2, we find that the delocalized screening charge is recovered for Co_S^- and C_S^- [cf. Fig. 3(b)]. While this is expected for localized defects in the bulk WS_2, the agreement found in the ML WS_2 is a compelling evidence that the localized defects therein are still subject to the bulklike screening and can be adequately described by α_G^{bulk}. The deviation from the ideal screening charge is more visible for V_S, in accord with its more delocalized nature and hence the larger deviation of α_K from α_G^{bulk} compared to the substitutional defects.

In contrast to α_K, the large α_G for the ML WS_2 is inherent to the strong opening of band gaps for 2D materials. We note in passing that the long-range part of Fock exchange is critical in opening the band gap of 2D materials given the asymptotic $1/r$ decay in vacuum. In fact, the short-ranged Heyd–Scuseria–Ernzerhof (HSE) functional [64] struggles to open up the band gap of the ML WS_2 unless an excessively large mixing parameter is used (0.45 with the PBE structure or 0.55 if the structure is relaxed self-consistently). However, such a large mixing parameter results in a highly distorted band structure (e.g., valence bandwidth) and, more importantly, shifts the whole band edges by -0.3 eV compared to G_0W_0 and PBE0(α_G) (see the SM). Nonetheless, for localized

defects, the HSE defect levels are reasonably aligned to the vacuum level as the short-range bulklike screening dominates.

In addition to the TMDs, we find that the distinct two-set values (α_K and α_G) also apply to the ML hexagonal boron nitride (h-BN) involving only simple sp elements (see the SM). While systems characterized by localized d electrons are less amenable to treatment for fulfilling the Koopmans' condition [54, 65], we emphasize that the non-uniqueness of α is a general attribute for hybrid-functional defect calculations in 2D materials.

Before closing, we note that our study focuses on defect energy levels. It remains an open question how the nonuniqueness of α affects other defect properties, such as the defect formation energies, the optical transitions, and the phonons. Our findings motivate further investigations of the possible implications for general defect physics in 2D materials.

In conclusion, we have shown that using a fixed amount of Fock exchange in hybrid functionals could lead to qualitatively incorrect description of defects in 2D materials, in contrast with the established practice common to defect calculations in bulk materials. The absence of a unique mixing parameter stems from the reduced screening for the delocalized band-edge states whereas the screening is bulklike for localized defects. The distinct screening behaviors hence require the band edges and the defect states to be treated separately through their own optimal mixing parameters. We expect these effects to be present in all 2D materials and they should be carefully taken into account to ensure accurate hybrid-functional defect computations.

This work was supported by the U.S. Department of Energy, Office of Science, Basic Energy Sciences in Quantum Information Science under Award Number DE-SC0022289. This research used resources of the National Energy Research Scientific Computing Center, a DOE Office of Science User Facility supported by the Office of Science of the U.S. Department of Energy under Contract No. DE-AC02-05CH11231 using NERSC award BES-ERCAP0020966. Computational resources were also provided by supercomputing facilities of UCLouvain (CISM) and Consortium des Equipements de Calcul Intensif en Fédération Wallonie-Bruxelles (CECI). The authors acknowledge Y. Ping, M. C. da Silva, and P. Deák for fruitful discussions.

[1] X. Duan, C. Wang, A. Pan, R. Yu, and X. Duan, Two-dimensional transition metal dichalcogenides as atomically thin semiconductors: opportunities and challenges, Chem. Soc. Rev. **44**, 8859 (2015).

[2] G. Ye, Y. Gong, J. Lin, B. Li, Y. He, S. T. Pantelides, W. Zhou, R. Vajtai, and P. M. Ajayan, Defects engineered monolayer MoS_2 for improved hydrogen evolution reaction, Nano Lett. **16**, 1097 (2016).

[3] Y. Ouyang, C. Ling, Q. Chen, Z. Wang, L. Shi, and J. Wang, Activating inert basal planes of MoS_2 for hydrogen evolution reaction through the formation of different intrinsic defects, Chem. Mater. **28**, 4390 (2016).

[4] C. Tsai, H. Li, S. Park, J. Park, H. S. Han, J. K. Nørskov, X. Zheng, and F. Abild-Pedersen, Electrochemical generation of sulfur vacancies in the basal plane of MoS_2 for hydrogen evolution, Nat. Commun. **8**, 15113 (2017).

[5] T. T. Tran, K. Bray, M. J. Ford, M. Toth, and I. Aharonovich, Quantum emission from hexagonal boron nitride monolayers, Nat. Nanotechnology **11**, 37 (2016).

[6] J. D. Caldwell, I. Aharonovich, G. Cassabois, J. H. Edgar, B. Gil, and D. N. Basov, Photonics with hexagonal boron nitride, Nat. Rev. Mater. **4**, 552 (2019).

[7] N. Mendelson, D. Chugh, J. R. Reimers, T. S. Cheng, A. Gottscholl, H. Long, C. J. Mellor, A. Zettl, V. Dyakonov, P. H. Beton, S. V. Novikov, C. Jagadish, H. H. Tan, M. J. Ford, M. Toth, C. Bradac, and I. Aharonovich, Identifying carbon as the source of visible single-photon emission from hexagonal boron nitride, Nat. Mater. **20**, 321 (2021).

[8] M. E. Turiansky, A. Alkauskas, L. C. Bassett, and C. G. Van de Walle, Dangling bonds in hexagonal boron nitride as single-photon emitters, Phys. Rev. Lett. **123**, 127401 (2019).

[9] Y. Ping and T. J. Smart, Computational design of quantum defects in two-dimensional materials, Nat. Comput. Sci. **1**, 646 (2021).

[10] C. Freysoldt, B. Grabowski, T. Hickel, J. Neugebauer, G. Kresse, A. Janotti, and C. G. Van de Walle, First-principles calculations for point defects in solids, Rev. Mod. Phys. **86**, 253 (2014).

[11] W. Chen and A. Pasquarello, Correspondence of defect energy levels in hybrid density functional theory and many-body perturbation theory, Phys. Rev. B **88**, 115104 (2013).

[12] J. P. Perdew, R. G. Parr, M. Levy, and J. L. Balduz, Density-functional theory for fractional particle number: Derivative discontinuities of the energy, Phys. Rev. Lett. **49**, 1691 (1982).

[13] S. Lany and A. Zunger, Polaronic hole localization and multiple hole binding of acceptors in oxide wide-gap semiconductors, Phys. Rev. B **80**, 085202 (2009).

[14] T. Stein, J. Autschbach, N. Govind, L. Kronik, and R. Baer, Curvature and frontier orbital energies in density functional theory, J. Phys. Chem. Lett. **3**, 3740 (2012).

[15] J. P. Perdew, W. Yang, K. Burke, Z. Yang, E. K. U. Gross, M. Scheffler, G. E. Scuseria, T. M. Henderson, I. Y. Zhang, A. Ruzsinszky, H. Peng, J. Sun, E. Trushin, and A. Görling, Understanding band gaps of solids in generalized Kohn-Sham theory, Proc. Natl. Acad. Sci. **114**, 2801 (2017).

[16] G. Miceli, W. Chen, I. Reshetnyak, and A. Pasquarello, Nonempirical hybrid functionals for band gaps and polaronic distortions in solids, Phys. Rev. B **97**, 121112(R) (2018).

[17] W.-F. Li, C. Fang, and M. A. van Huis, Strong spin-orbit splitting and magnetism of point defect states in monolayer WS_2, Phys. Rev. B **94**, 195425 (2016).

[18] T. J. Smart, F. Wu, M. Govoni, and Y. Ping, Fundamental principles for calculating charged defect ionization energies in ultrathin two-dimensional materials, Phys. Rev.

Materials **2**, 124002 (2018).
[19] S. Li, G. Thiering, P. Udvarhelyi, V. Ivády, and A. Gali, Carbon defect qubit in two-dimensional WS_2, Nat. Commun. **13**, 1210 (2022).
[20] K. Li, T. J. Smart, and Y. Ping, Carbon trimer as a 2 eV single-photon emitter candidate in hexagonal boron nitride: A first-principles study, Phys. Rev. Materials **6**, L042201 (2022).
[21] Y.-M. He, G. Clark, J. R. Schaibley, Y. He, M.-C. Chen, Y.-J. Wei, X. Ding, Q. Zhang, W. Yao, X. Xu, C.-Y. Lu, and J.-W. Pan, Single quantum emitters in monolayer semiconductors, Nat. Nanotechnology **10**, 497 (2015).
[22] A. Srivastava, M. Sidler, A. V. Allain, D. S. Lembke, A. Kis, and A. Imamoğlu, Optically active quantum dots in monolayer WSe_2, Nat. Nanotechnology **10**, 491 (2015).
[23] M. Koperski, K. Nogajewski, A. Arora, V. Cherkez, P. Mallet, J.-Y. Veuillen, J. Marcus, P. Kossacki, and M. Potemski, Single photon emitters in exfoliated WSe_2 structures, Nat. Nanotechnology **10**, 503 (2015).
[24] C. Chakraborty, L. Kinnischtzke, K. M. Goodfellow, R. Beams, and A. N. Vamivakas, Voltage-controlled quantum light from an atomically thin semiconductor, Nat. Nanotechnology **10**, 507 (2015).
[25] C. Palacios-Berraquero, D. M. Kara, A. R.-P. Montblanch, M. Barbone, P. Latawiec, D. Yoon, A. K. Ott, M. Loncar, A. C. Ferrari, and M. Atatüre, Large-scale quantum-emitter arrays in atomically thin semiconductors, Nat. Commun. **8**, 15093 (2017).
[26] B. Schuler, K. A. Cochrane, C. Kastl, E. S. Barnard, E. Wong, N. J. Borys, A. M. Schwartzberg, D. F. Ogletree, F. J. G. de Abajo, and A. Weber-Bargioni, Electrically driven photon emission from individual atomic defects in monolayer WS_2, Sci. Adv. **6**, eabb5988 (2020).
[27] B. Schuler, D. Y. Qiu, S. Refaely-Abramson, C. Kastl, C. T. Chen, S. Barja, R. J. Koch, D. F. Ogletree, S. Aloni, A. M. Schwartzberg, J. B. Neaton, S. G. Louie, and A. Weber-Bargioni, Large spin-orbit splitting of deep in-gap defect states of engineered sulfur vacancies in monolayer WS_2, Phys. Rev. Lett. **123**, 076801 (2019).
[28] F. Zhang, Y. Lu, D. S. Schulman, T. Zhang, K. Fujisawa, Z. Lin, Y. Lei, A. L. Elias, S. Das, S. B. Sinnott, and M. Terrones, Carbon doping of WS_2 monolayers: Bandgap reduction and p-type doping transport, Sci. Adv. **5**, eaav5003 (2019).
[29] K. A. Cochrane, J.-H. Lee, C. Kastl, J. B. Haber, T. Zhang, A. Kozhakhmetov, J. A. Robinson, M. Terrones, J. Repp, J. B. Neaton, A. Weber-Bargioni, and B. Schuler, Spin-dependent vibronic response of a carbon radical ion in two-dimensional WS_2, Nat. Commun. **12**, 7287 (2021).
[30] J. P. Perdew, K. Burke, and M. Ernzerhof, Generalized gradient approximation made simple, Phys. Rev. Lett. **77**, 3865 (1996).
[31] J. P. Perdew, M. Ernzerhof, and K. Burke, Rationale for mixing exact exchange with density functional approximations, J. Chem. Phys. **105**, 9982 (1996).
[32] C. Adamo and V. Barone, Toward reliable density functional methods without adjustable parameters: The PBE0 model, J. Chem. Phys. **110**, 6158 (1999).
[33] P. E. Blöchl, Projector augmented-wave method, Phys. Rev. B **50**, 17953 (1994).
[34] G. Kresse and J. Furthmüller, Efficiency of ab-initio total energy calculations for metals and semiconductors using a plane-wave basis set, Comput. Mater. Sci. **6**, 15 (1996).
[35] G. Kresse and J. Furthmüller, Efficient iterative schemes for ab initio total-energy calculations using a plane-wave basis set, Phys. Rev. B **54**, 11169 (1996).
[36] L. Hedin, New method for calculating the one-particle green's function with application to the electron-gas problem, Phys. Rev. **139**, A796 (1965).
[37] M. S. Hybertsen and S. G. Louie, Electron correlation in semiconductors and insulators: Band gaps and quasiparticle energies, Phys. Rev. B **34**, 5390 (1986).
[38] S. Ismail-Beigi, Truncation of periodic image interactions for confined systems, Phys. Rev. B **73**, 233103 (2006).
[39] F. H. da Jornada, D. Y. Qiu, and S. G. Louie, Nonuniform sampling schemes of the Brillouin zone for many-electron perturbation-theory calculations in reduced dimensionality, Phys. Rev. B **95**, 035109 (2017).
[40] D. Y. Qiu, F. H. da Jornada, and S. G. Louie, Screening and many-body effects in two-dimensional crystals: Monolayer MoS_2, Phys. Rev. B **93**, 235435 (2016).
[41] J. Deslippe, G. Samsonidze, D. A. Strubbe, M. Jain, M. L. Cohen, and S. G. Louie, BerkeleyGW: A massively parallel computer package for the calculation of the quasiparticle and optical properties of materials and nanostructures, Comput. Phys. Commun. **183**, 1269 (2012).
[42] P. Giannozzi, O. Andreussi, T. Brumme, O. Bunau, M. B. Nardelli, M. Calandra, R. Car, C. Cavazzoni, D. Ceresoli, M. Cococcioni, N. Colonna, I. Carnimeo, A. D. Corso, S. de Gironcoli, P. Delugas, R. A. DiStasio, A. Ferretti, A. Floris, G. Fratesi, G. Fugallo, R. Gebauer, U. Gerstmann, F. Giustino, T. Gorni, J. Jia, M. Kawamura, H.-Y. Ko, A. Kokalj, E. Küçükbenli, M. Lazzeri, M. Marsili, N. Marzari, F. Mauri, N. L. Nguyen, H.-V. Nguyen, A. O. de-la Roza, L. Paulatto, S. Poncé, D. Rocca, R. Sabatini, B. Santra, M. Schlipf, A. P. Seitsonen, A. Smogunov, I. Timrov, T. Thonhauser, P. Umari, N. Vast, X. Wu, and S. Baroni, Advanced capabilities for materials modelling with Quantum espresso, J. Phys.: Condens. Matter **29**, 465901 (2017).
[43] See Supplemental Material for computational details, finite-size corrections, and Koopmans' condition with monolayer boron nitride, which includes Refs.[66–70].
[44] A. Chernikov, T. C. Berkelbach, H. M. Hill, A. Rigosi, Y. Li, O. B. Aslan, D. R. Reichman, M. S. Hybertsen, and T. F. Heinz, Exciton binding energy and nonhydrogenic rydberg series in monolayer WS_2, Phys. Rev. Lett. **113**, 076802 (2014).
[45] B. Zhu, X. Chen, and X. Cui, Exciton binding energy of monolayer WS_2, Sci. Rep. **5**, 9218 (2015).
[46] M. H. Naik and M. Jain, Substrate screening effects on the quasiparticle band gap and defect charge transition levels in MoS_2, Phys. Rev. Mater. **2**, 084002 (2018).
[47] N. Zibouche, M. Schlipf, and F. Giustino, *GW* band structure of monolayer MoS_2 using the sternheimergw method and effect of dielectric environment, Phys. Rev. B **103**, 125401 (2021).
[48] C. Freysoldt, J. Neugebauer, and C. G. Van de Walle, Fully ab initio finite-size corrections for charged-defect supercell calculations, Phys. Rev. Lett. **102**, 016402 (2009).
[49] H.-P. Komsa, T. T. Rantala, and A. Pasquarello, Finite-size supercell correction schemes for charged defect calculations, Phys. Rev. B **86**, 045112 (2012).
[50] H.-P. Komsa and A. Pasquarello, Finite-size supercell correction for charged defects at surfaces and interfaces,

Phys. Rev. Lett. **110**, 095505 (2013).
[51] M. Chagas da Silva, M. Lorke, B. Aradi, M. Farzalipour Tabriz, T. Frauenheim, A. Rubio, D. Rocca, and P. Deák, Self-consistent potential correction for charged periodic systems, Phys. Rev. Lett. **126**, 076401 (2021).
[52] F. Bruneval, *GW* approximation of the many-body problem and changes in the particle number, Phys. Rev. Lett. **103**, 176403 (2009).
[53] T. Bischoff, I. Reshetnyak, and A. Pasquarello, Adjustable potential probes for band-gap predictions of extended systems through nonempirical hybrid functionals, Phys. Rev. B **99**, 201114(R) (2019).
[54] J. Yang, S. Falletta, and A. Pasquarello, One-shot approach for enforcing piecewise linearity on hybrid functionals: Application to band gap predictions, J. Phys. Chem. Lett. **13**, 3066 (2022).
[55] P. Deák, M. Lorke, B. Aradi, and T. Frauenheim, Optimized hybrid functionals for defect calculations in semiconductors, J. Appl. Phys. **126**, 130901 (2019).
[56] H.-P. Komsa, N. Berseneva, A. V. Krasheninnikov, and R. M. Nieminen, Charged point defects in the flatland: Accurate formation energy calculations in two-dimensional materials, Phys. Rev. X **4**, 031044 (2014); Erratum: Charged point defects in the flatland: Accurate formation energy calculations in two-dimensional materials [Phys. Rev. X 4, 031044 (2014)], Phys. Rev. X **8**, 039902(E) (2018).
[57] M. Farzalipour Tabriz, B. Aradi, T. Frauenheim, and P. Deák, SLABCC: Total energy correction code for charged periodic slab models, Comput. Phys. Commun. **240**, 101 (2019).
[58] A. Alkauskas, P. Broqvist, and A. Pasquarello, Defect energy levels in density functional calculations: Alignment and band gap problem, Phys. Rev. Lett. **101**, 046405 (2008).
[59] H.-P. Komsa, P. Broqvist, and A. Pasquarello, Alignment of defect levels and band edges through hybrid functionals: Effect of screening in the exchange term, Phys. Rev. B **81**, 205118 (2010).
[60] C. Freysoldt, B. Lange, J. Neugebauer, Q. Yan, J. L. Lyons, A. Janotti, and C. G. Van de Walle, Electron and chemical reservoir corrections for point-defect formation energies, Phys. Rev. B **93**, 165206 (2016).
[61] J. L. Lyons and C. G. Van de Walle, Computationally predicted energies and properties of defects in GaN, npj Comput. Mater. **3**, 12 (2017).
[62] K. K. Kam and B. A. Parkinson, Detailed photocurrent spectroscopy of the semiconducting group VIB transition metal dichalcogenides, J. Phys. Chem. **86**, 463 (1982).
[63] J. Gusakova, X. Wang, L. L. Shiau, A. Krivosheeva, V. Shaposhnikov, V. Borisenko, V. Gusakov, and B. K. Tay, Electronic properties of bulk and monolayer TMDs: Theoretical study within dft framework (GVJ-2e method), Phys. Status Solidi A **214**, 1700218 (2017).
[64] J. Heyd, G. E. Scuseria, and M. Ernzerhof, Hybrid functionals based on a screened coulomb potential, J. Chem. Phys. **118**, 8207 (2003).
[65] V. Ivády, I. A. Abrikosov, E. Janzén, and A. Gali, Role of screening in the density functional applied to transition-metal defects in semiconductors, Phys. Rev. B **87**, 205201 (2013).
[66] W. Schutte, J. de Boer, and F. Jellinek, Crystal structures of tungsten disulfide and diselenide, J. Solid State Chem. **70**, 207 (1987).
[67] L. Lin, Adaptively compressed exchange operator, J. Chem. Theory Comput. **12**, 2242 (2016).
[68] D. R. Hamann, Optimized norm-conserving Vanderbilt pseudopotentials, Phys. Rev. B **88**, 085117 (2013).
[69] M. van Setten, M. Giantomassi, E. Bousquet, M. Verstraete, D. Hamann, X. Gonze, and G.-M. Rignanese, The PSEUDODOJO: Training and grading a 85 element optimized norm-conserving pseudopotential table, Comput. Phys. Commun. **226**, 39 (2018).
[70] R. W. Godby and R. J. Needs, Metal-insulator transition in Kohn-Sham theory and quasiparticle theory, Phys. Rev. Lett. **62**, 1169 (1989).

Supplemental Material
Non-unique fraction of Fock exchange for defects in two-dimensional materials

Wei Chen,[1] Sinéad M. Griffin,[2,3] Gian-Marco Rignanese,[1] and Geoffroy Hautier[1,4]

[1] *Institute of Condensed Matter and Nanoscicence (IMCN), Université catholique de Louvain, Louvain-la-Neuve 1348, Belgium*
[2] *Molecular Foundry Division, Lawrence Berkeley National Laboratory, Berkeley, California 94720, USA*
[3] *Materials Sciences Division, Lawrence Berkeley National Laboratory, Berkeley, California 94720, USA*
[4] *Thayer School of Engineering, Dartmouth College, Hanover, New Hampshire 03755, USA*

(Dated: October 11, 2022)

COMPUTATIONAL DETAILS

We employ two orthorhombic supercells to represent the monolayer (ML) WS_2. The majority of hybrid functionals are carried out with the 90-atom orthorhombic supercell by transforming the in-plane lattice vectors of the primitive cell through the matrix $\left(\begin{smallmatrix} 5 & 5 \\ -3 & 3 \end{smallmatrix}\right)$. The out-of-plane lattice parameter $L_z = 24$ Å. A smaller 36-atom orthorhombic supercell is obtained via the transformation matrix $\left(\begin{smallmatrix} 3 & 3 \\ -2 & 2 \end{smallmatrix}\right)$ with $L_z = 16$ Å. The smaller supercell is used in G_0W_0 calculations and for analyzing the finite-size effect. The experimental in-plane lattice constant of the bulk $2H$-WS_2 ($a = 3.15$ Å [1]) is used without further relaxation for the ML WS_2.

The kinetic energy cutoff is 340 eV for the projector-augmented wave (PAW) calculations. For the carbon substitutional defect (C_S), the cutoff is increased to 400 eV. We use a k-point mesh density equivalent to $12\times12\times1$ for the primitive cell of ML WS_2 (e.g., $4\times4\times1$ for the 36-atom supercell and $3\times3\times1$ for the 90-atom supercell). The evaluation of Fock exchange is sped up with the adaptively compressed exchange operator formulation [2] with an energy cutoff of 270 eV (320 eV for C_S). The atomic coordinates are relaxed until the residual forces are below 0.02 eV/Å.

The mean-field starting point for the one-shot G_0W_0 calculations are carried out using the optimized norm-conserving pseudopotentials [3] made available via the PseudoDojo project [4]. We use the $4\times4\times1$ Γ-centered k-point mesh for the 36-atom orthorhombic supercell. The dielectric matrix is evaluated with up to 5000 bands and a planewave energy cutoff of 10 Ry. Frequency dependence of dielectric function is taken into account by the Godby-Needs plasmon-pole model [5]. The truncated Coulomb interaction is applied along the out-of-plane direction [6]. The slow convergence with respect to q points is addressed by the subsampling technique [7], which includes 3 additional q points for $q \to 0$. Spin-orbit coupling is not included in G_0W_0 calculations.

We find the QP energies can be reasonably described with a smaller orthorhombic supercell of 36 atoms owing to the strong localization of the defect. For results depicted in Fig. 2(a) of the main text, we use the PBE equilibrium configuration of the neutral defect and refrain from further relaxations for the negatively charged defect in order to exclude the structural effect.

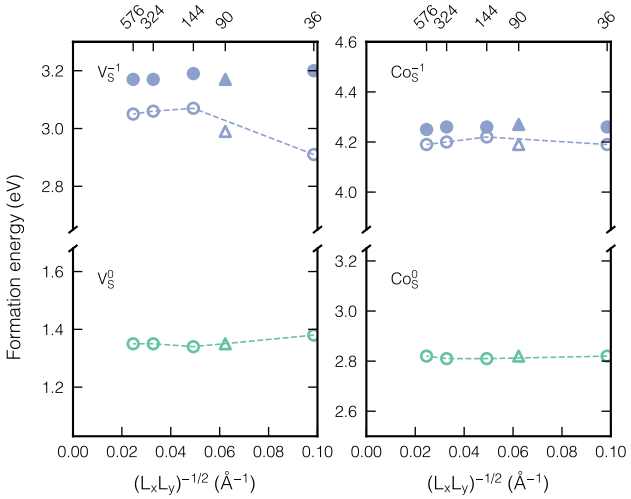

FIG. S1. Uncorrected and corrected formation energies for the V_S and Co_S defects calculated with DFT-PBE. For the series of supercells with 36, 144, 324, and 576 atoms (denoted by circles) the supercell length $L_z = 1.6(L_xL_y)^{1/2}$. For the 90-atom supercell (denoted by triangles) $L_z = 1.5(L_xL_y)^{1/2}$. For the charged defects, the uncorrected (corrected) formation energies are shown by the empty (filled) circles.

FINITE-SIZE CORRECTIONS

The total energies of charged point defects are corrected by the *a posteriori* correction scheme [8–10]. Since ionic contributions to the dielectric screening is negligible for WS_2, we use the high-frequency dielectric constant throughout. Figure S1 shows the formation energies of V_S and Co_S in the ML WS_2. Co_S exhibits strongly localized defect wavefunctions whereas V_S is less localized. Overall the corrected formation energies for the charged defects are converged already with the 36-atom supercell regardless of defect localization.

For charged defects in the ML WS_2, the electrostatic potential and eigenvalues are corrected concurrently using the scheme of Chagas da Silva *et al.* [11]. Figure S2

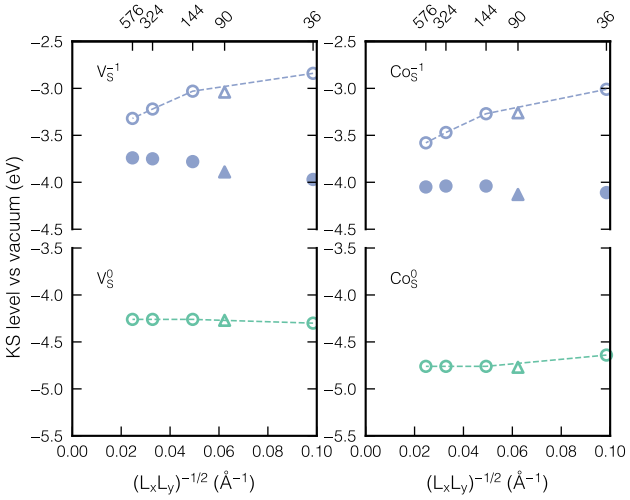

FIG. S2. Uncorrected and corrected KS single-particle eigenvalues with respect to the vacuum level calculated with DFT-PBE.

shows the Kohn-Sham (KS) single-particle eigenvalues associated with V_S and Co_S. The electrostatic potential furthest away from the defect is taken as the vacuum reference level. While the single-particle eigenvalues are well defined for the neutral defects, they are subject to strong finite size effect as the supercell size varies. The potential correction scheme works well for the negatively charged Co_S^- and the corrected eigenvalue is already converged within 0.1 eV with the smallest 36-atom supercell. For V_S^- the slower convergence of the corrected eigenvalues can be attributed to the more delocalized nature of the defect wavefunctions. Nonetheless, the eigenvalue of V_S^- is still reasonably converged within 0.2 eV with the 36-atom supercell.

For defects in the bulk WS_2, we apply the eigenvalue correction $-\frac{2}{q}E_{\rm corr}$ where $E_{\rm corr}$ is the total-energy correction [12].

EFFECT OF STRUCTURAL RELAXATIONS

In Fig. 2a of the main text, the single-particle defect levels are obtained using the neutral charge defect structures relaxed at the PBE level. Here we investigate the effect of structural relaxations on the single-particle defect levels. Taking Co_S^0 for example, we show in Table S1 that relaxing the structure using PBE0($\alpha_{\rm K}=0.06$) increases the Co–W bond lengths by 0.02 Åunder the C_S symmetry. The slighlt modification in the defect structure leads to a marginal shift of the defect energy level by 0.04 eV.

We note that the comparison as done in Fig. 2a is nonethless unaffected by the choice of the reference structure.

TABLE S1. Difference in the nearest Co–W bond lengths and in the single-particle defect level due to the choice of the reference Co_S^0 structure. The two structures, referred to as R(α), correspond to the equilibrium structure obtained with PBE0(α). The single-particle defect level is evaluated with PBE0($\alpha_{\rm K}=0.06$) and is referred to the vacuum level.

R(α)	$d_{\rm Co-W_1}$ (Å)	$d_{\rm Co-W_{2,3}}$ (Å)	$\epsilon^{\rm HO}(-)$ (eV)
R(0)	2.48	2.52	-4.16
R($\alpha_{\rm K}=0.06$)	2.50	2.54	-4.12

ROLE OF LONG-RANGE FOCK EXCHANGE FOR 2D SYSTEMS

The range-separated HSE hybrid functional only retains the Fock exchange in the short range. This is practical for 3D semiconductors as it accelerates the computation, but for 2D systems the short-range hybrid functional is insufficient to account for the band-gap opening at the reduced dimension. While it is in principle possible to recover the band gap with an exceedingly large α in HSE, the band structure is visibly distorted. This is manifested, for instance, by the too large VBM bandwidth and the overestimated direct band gap at Γ (cf. Fig. S3). On the other hand, the band structure of PBE0($\alpha_{\rm G}$) is in much better agreement with the G_0W_0 one. In addition, the large α places the HSE band edges about 0.3 eV too deep compared to the G_0W_0, PBE0($\alpha_{\rm G}$) again achieves an excellent agreement in terms of the absolution band-edge positions.

The too deep VBM has an implication for interpreting defect levels when referenced to the band edges. As shown in Fig. S5, the HSE single-particle defect level of Co_S^- is about 0.3 eV higher than those of PBE0 and G_0W_0 as a result of the misaligned VBM. Nevertheless, HSE still leads to consistent descriptions of defect levels insofar as the vacuum level is used as the common reference.

Figure S4 shows the single-particle defect levels as a function of α with the range-separated HSE functional. We obtain $\alpha_{\rm K}=0.21$ for $V_S^{0/-}$ and $\alpha_{\rm K}=0.07$ for $Co_S^{0/-}$. In accord with the PBE0 results, these values are considerably smaller than the $\alpha_{\rm G}$ (0.55). The sizable discrepancy between $\alpha_{\rm K}$ and $\alpha_{\rm G}$ is therefore universal for 2D materials regardless of range separation.

KOOPMANS' CONDITION AND SPIN-ORBIT COUPLING

The values of $\alpha_{\rm K}$ (i.e., the mixing parameter fulfilling the Koopmans' condition) have been determined without taking into account spin-orbit coupling (SOC) in the main text. We show in Table S2 that Koopmans' condition is still largely fulfilled at these $\alpha_{\rm K}$ values if the SOC is taken into account. In particular, the two single-

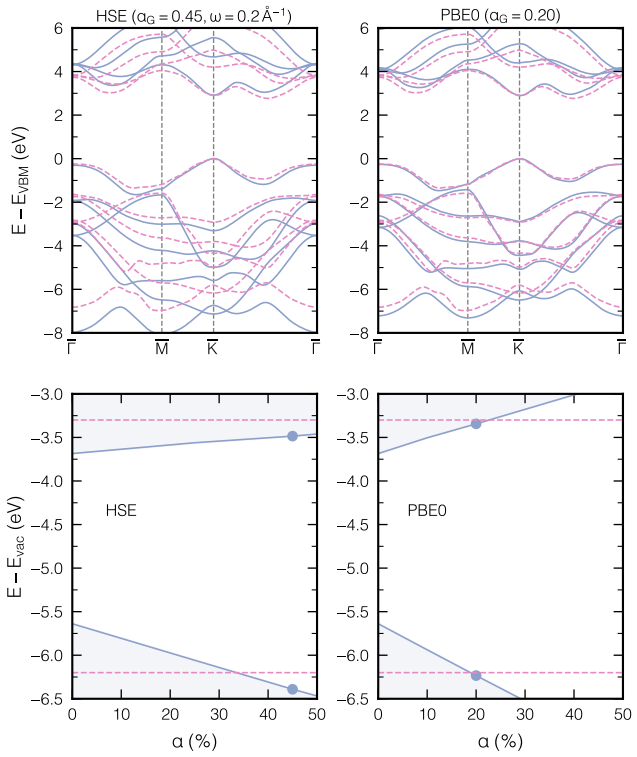

FIG. S3. Band structure of ML WS_2 (top panel) and absolute band-edge positions (bottom) obtained with the short-range hybrid functional (HSE) and the global hybrid functional retaining the long-range part of the Fock exchange (PBE0). In the band-structure plot both functionals use a mixing parameter α leading to the G_0W_0 band gap. The G_0W_0 band structure is shown in dashed lines. The energy is referred to the top of the VBM at K. The band-edge positions are shown as a function of the mixing parameter α. The α value at which the G_0W_0 band gap is reproduced is highlighted. The G_0W_0 band-edge positions are indicated by the dashed lines.

TABLE S2. Single-particle eigenvalues (in eV) of the pertinent defect states with respect to the vacuum level including the SOC effect. The fraction of Fock exchange at which the eigenvalues are evaulated follows the α_K values from the main text without taking into account SOC. For any given defect, the equilibrium structure of the charged defect does not include the SOC effect and is used for the neutral one.

	V_S^{-1}	C_S^{-1}	Co_W^{-1}	Co_W^{+1}	Co_S^{-1}	Co_S^{+1}
$\varepsilon(q)$	−4.25	−4.81	−4.69	−5.23	−4.17	−5.23
$\varepsilon(0)$	−4.18	−4.88	−4.76	−5.32	−4.26	−5.23

particle eigenvalues agree within 0.1 eV for all the defects considered in this work.

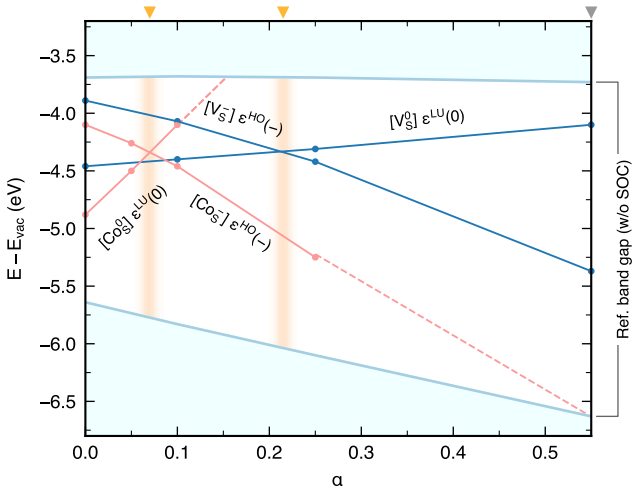

FIG. S4. Single-particle defect levels as a function of α with the range-separated HSE functional. The inverse screening length is set to 0.2 Å^{-1}. For legends refer to Fig. 1 of the main text.

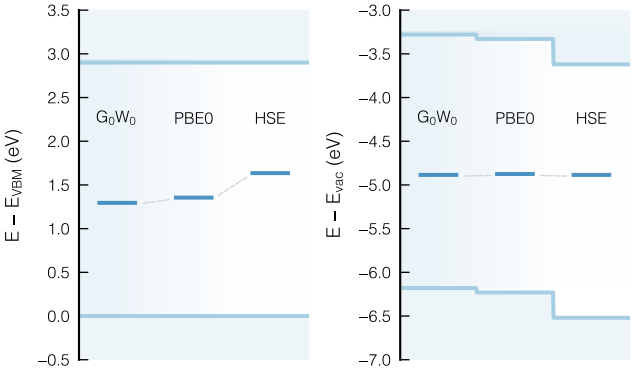

FIG. S5. Single-particle defect level of Co_S^- calculated with two families of hybrid functionals (PBE0 and HSE) and compared to G_0W_0 reference. The defect levels are referred to the VBM (left) and to the vacuum level (right). For the hybrid functionals, the band edges are obtained with the optimal mixing parameter (α_G) which reproduces the G_0W_0 band gap, whereas the defect levels are determined by the mixing parameter (α_K) fulfilling Koopmans' condition. Concretely, α_G is 0.22 (0.55) for PBE0 (HSE), and α_K is 0.07 (0.07) for PBE0 (HSE). The inverse screening length is fixed at 0.2 Å^{-1} for HSE.

KOOPMANS' CONDITION FOR MONOLAYER BORON NITRIDE

We extend the analysis to the hexagonal boron nitride (h-BN), a simple sp semiconductor. We use the C_N substitutional defect to probe to what extent the Koopmans' condition is fulfilled at given α values. The band gap of the ML h-BN, which corresponds to the indirect $K-\Gamma$ transition, is 7.0 eV according to the G_0W_0 calculations of Ref. [13]. To reproduce this G_0W_0 band gap, the mix-

TABLE S3. Highest occupied eigenvalues of the negatively charged C_N^- [$\varepsilon^{HO}(-)$] and lowest unoccupied eigenvalues of the neutral C_N^0 [$\varepsilon^{LU}(0)$] obtained with α_G^{ML} along with a vanishing α value and the standard $\alpha = 0.25$. The equilibrium structure of C_N^- obtained with the PBE functional is used throughout. The eigenvalues are referred to the vacuum level and are in eV. The deviation from piecewise linearity is indicated by Δ. A positive (negative) Δ value corresponds to convexity (concavity).

	$\alpha = 0$	$\alpha = 0.25$	$\alpha_G^{ML} = 0.35$
$\varepsilon^{HO}(-)$	−3.50	−4.34	−4.70
$\varepsilon^{LU}(0)$	−5.11	−4.42	−4.08
Δ	1.61	0.08	−0.62

ing parameter α_G^{ML} of 0.35 is needed for the PBE0 hybrid functional. In comparison, the standard PBE0($\alpha = 0.25$) describes the band gap of the bulk h-BN reasonably well.

The defect calculations are carried out with a 72-atom orthorhombic supercell with $L_z = 15$ Å using an energy cutoff of 400 eV and a Γ-centered $4 \times 4 \times 4$ **k**-point mesh. Table S3 shows the highest occupied and the lowest unoccupied eigenvalues pertinent to the determination of Koopmans' condition at three representative α values, namely 0, 0.25, and α_G^{ML}. As expected, the Koopmans' condition is best satisfied at $\alpha = 0.25$, the value closely reproducing the band gap of the bulk h-BN. The other two values lead to either strong convexity or strong concavity. The Koopmans' α_K value is estimated to be 0.26, significantly lower than the α_G^{ML}. This shows that the non-uniqueness of α is a general attribute applicable to a wide class of 2D materials.

DATA AVAILABILITY

The input and output files for the defect calculations presented in this work are available at https://doi.org/10.5281/zenodo.6916999.

[1] W. Schutte, J. de Boer, and F. Jellinek, Crystal structures of tungsten disulfide and diselenide, J. Solid State Chem. **70**, 207 (1987).

[2] L. Lin, Adaptively compressed exchange operator, J. Chem. Theory Comput. **12**, 2242 (2016).

[3] D. R. Hamann, Optimized norm-conserving Vanderbilt pseudopotentials, Phys. Rev. B **88**, 085117 (2013).

[4] M. van Setten, M. Giantomassi, E. Bousquet, M. Verstraete, D. Hamann, X. Gonze, and G.-M. Rignanese, The PseudoDojo: Training and grading a 85 element optimized norm-conserving pseudopotential table, Comput. Phys. Commun. **226**, 39 (2018).

[5] R. W. Godby and R. J. Needs, Metal-insulator transition in kohn-sham theory and quasiparticle theory, Phys. Rev. Lett. **62**, 1169 (1989).

[6] S. Ismail-Beigi, Truncation of periodic image interactions for confined systems, Phys. Rev. B **73**, 233103 (2006).

[7] F. H. da Jornada, D. Y. Qiu, and S. G. Louie, Nonuniform sampling schemes of the brillouin zone for many-electron perturbation-theory calculations in reduced dimensionality, Phys. Rev. B **95**, 035109 (2017).

[8] H.-P. Komsa and A. Pasquarello, Finite-size supercell correction for charged defects at surfaces and interfaces, Phys. Rev. Lett. **110**, 095505 (2013).

[9] H.-P. Komsa, N. Berseneva, A. V. Krasheninnikov, and R. M. Nieminen, Charged point defects in the flatland: Accurate formation energy calculations in two-dimensional materials, Phys. Rev. X **4**, 031044 (2014).

[10] M. Farzalipour Tabriz, B. Aradi, T. Frauenheim, and P. Deák, SLABCC: Total energy correction code for charged periodic slab models, Comput. Phys. Commun. **240**, 101 (2019).

[11] M. Chagas da Silva, M. Lorke, B. Aradi, M. Farzalipour Tabriz, T. Frauenheim, A. Rubio, D. Rocca, and P. Deák, Self-consistent potential correction for charged periodic systems, Phys. Rev. Lett. **126**, 076401 (2021).

[12] W. Chen and A. Pasquarello, Correspondence of defect energy levels in hybrid density functional theory and many-body perturbation theory, Phys. Rev. B **88**, 115104 (2013).

[13] T. J. Smart, F. Wu, M. Govoni, and Y. Ping, Fundamental principles for calculating charged defect ionization energies in ultrathin two-dimensional materials, Phys. Rev. Materials **2**, 124002 (2018).